Nanoscale

PAPER

Luminomagnetic bifunctionality of Mn²⁺-bonded graphene oxide/reduced graphene oxide two dimensional nanosheets†

Amandeep,‡[a] Garima Kedawat,‡[b] Pawan Kumar,[a,c] Avaneesh Anshul,[a,d] Abhay D. Deshmukh,[a,e] Om Pal Singh,[a,c] R. K. Gupta,[f] S. S. Amritphale,[d] Govind Gupta,[a] V. N. Singh[a] and Bipin Kumar Gupta*[a]

Herein, we report the luminomagnetic bifunctional properties of two-dimensional (2D) Mn²⁺ bonded graphene oxide (GO)/reduced graphene oxide (RGO) nanosheets synthesized using a facile route of oxidation followed by a solvothermal reduction method. Photoluminescence (PL) studies (excited by different wavelengths) revealed that the resonant energy transfer between Mn²⁺ and sp^3/sp^2 clusters of GO/RGO is responsible for the enhancement of emissions. Moreover, pH-sensitive PL behaviors have also been investigated in detail. The ferromagnetic behavior is believed to arise due to defects in Mn²⁺ bonded GO composites. Thus, present reduction method provides a direct route to tune and enhance the optical properties of GO and RGO nanosheets bonded with Mn²⁺ ions, which creates an opportunity for various technological applications.

1. Introduction

Graphene with a honeycomb lattice has proven to be a new wonder material because of its applications in almost all branches of emerging science and technology.[1] Despite intense interest and extensive studies, achieving luminescence from zero band gap graphene is limited by its poor solubility. Graphene oxide (GO) is an atomically thin sheet of graphite which has traditionally served as a precursor for graphene. It is covalently decorated with oxygen and/or oxygen-containing functional groups at both the basal planes and edges.[2] It shows a good range of solubility in water and other oxygenic solvents, which allows it to be easily deposited onto a wide range of substrates.[3] Recently, luminescent GO has attracted research interest in optoelectronics and biological applications due to its tunable optical properties.[4–6] Reduced graphene

oxide (RGO), characterized as an incompletely reduced product of GO, is an intermediate product between graphene and GO. The unique chemical structure of GO and RGO along with their heterogeneous electronic structures (due to the presence of sp^2 and sp^3 bonding) confers exciting prospects for new applications. Both RGO and GO reveal a bandgap that can be tuned over a large range of energies, suggesting that the functionalization of graphene by oxidation can modify its optical, mechanical, and electrical properties[7,8] and can also change the various photoluminescence (PL) features.[9]

The chemically functionalized GO and RGO exhibit a broad luminescence emission from ultraviolet to near infrared.[4,9] The PL emission of GO is a quasi-molecule fluorescence[10] and it is also affected by various factors such as pH value[11] and the solvent[12] used for chemical reduction.[13] The fluorescence of GO over a wide range of wavelengths offers possibilities for incorporation into blue light-emitting diodes, white light emission for solid-state lighting and display applications on flexible platforms.[14] The low-energy fluorescence of GO or graphene quantum dots in red to near infrared (NIR) wavelengths is useful for biological applications.[16] In addition, mechanically exfoliated single-layer graphene has shown broad luminescence from 400 to 800 nm.[15] Red-to-near-infrared PL emitted from chemically-reduced GO is consistent with increasing disorder length scale with reduction.[16] The red emission in GO is due to a disorder-induced localized state related transition.[4] Moreover, the blue emission in GO is also reported from electron–hole recombination among sp^2 clusters enclosed by sp^3 defects.[17] The RGO and graphene quantum dots have also

[a]CSIR-National Physical Laboratory, Dr K S Krishnan Road, New Delhi, 110012, India. E-mail: bipinbhu@yahoo.com; Fax: +91-11-45609310; Tel: +91-11-45609385
[b]Department of Physics, Kalindi College, University of Delhi, New Delhi, 110008, India
[c]Academy of Scientific and Innovative Research (AcSIR), CSIR-National Physical Laboratory campus, New Delhi-110012, India
[d]CSIR-Advanced Materials and Processes Research Institute, Bhopal, 462024, India
[e]Energy Material and Devices Laboratory, Department of Physics, RTM Nagpur University, Nagpur, 440033, India
[f]Department of Chemistry, Pittsburg State University, Pittsburg, KS, 66762, USA
†Electronic supplementary information (ESI) available. See DOI: 10.1039/c5nr01095k
‡Both authors have equally contributed.

demonstrated blue fluorescence with a relatively narrow bandwidth.[17,18] The PL emission of GO can be tuned from red to blue by changing the amount of sp^2- and sp^3-bonded carbon atoms through the reduction of oxygen containing functional groups at the surface.[4] An excitation wavelength dependent PL with a strong blue emission is achieved from graphene quantum dots synthesized by cutting the preoxidized graphene sheets.[18] This blue luminescence may have originated from free zigzag sites of a carbene-like triplet ground state. The PL peak shifted to a slightly longer blue wavelength (with decreasing intensity), when the excitation wavelength was changed from 320 to 420 nm.

A further elucidation of the oxygen-related defects in graphene is important for exploring a new approach for tuning the energy band structure of graphene *via* defect engineering. In addition, the accessibility of the graphene surface also provides a unique opportunity to support chemical impurities that can modify the electronic and optical properties of graphene. Metal oxides can be uniformly dispersed on the plane of graphene and the charge transfer at the interface of these hybrid materials can show a synergistic effect to induce properties that are different from those of each individual components.[19–21] Recently, chemically modified fluorescent GO with *n*-butylamine has shown PL emission in which the maximum emission shifted towards the higher wavelength. The emission intensity decreased when the excitation wavelength was varied from 350 to 470 nm.[22] The intensity of long-wavelength PL was very weak despite the large scale distribution of sp^2 clusters. Gan *et al.* reported that MnO_2-decorated RGO demonstrated tunable and enhanced PL in a broad wavelength range (400–550 nm) due to the resonant energy transfer between Mn^{2+} and sp^2 clusters.[23] Li *et al.* proposed an excitation-independent blue emission with two stationary PLE peaks around 330 nm and 450 nm, which were due to the transfer of mediated energy from Mn^{2+} ions to the sp^2 carbon clusters, yielding an intense long-wavelength PL emission.[24]

In addition to this, magnetism of carbon based materials (graphene and its derivatives) is of particular interest, as the light weight magnets could open up new ways to design adaptable and flexible information storage systems.[25] The potential application of carbon-based magnets is in spin electronics because graphene has an extraordinary carrier mobility and this provides a way to integrate spin and molecular electronics easily.[26] These materials are also paid attention in biophysical and chemical sciences; since the spin dependent part of the electronic wave-function can affect the chemical bonding pathway. It is well-known that the ideal graphene is intrinsically non-magnetic, due to a de-localized π bonding network, which limits its applications in spintronics.[27] The spin orientation in GO has been introduced through topological defects, vacancies and doping of 3d and 4f elements.[28] The room temperature magnetism adds an extra degree of freedom in their potential functionalities and functional groups attached to a graphene skeleton also provides a higher net magnetization.[29] Low temperature ferromagnetism was reported in GO.[30] The ferromagnetic ordering in GO and RGO (lower oxygen concentration, higher vacancies and disorder) persist at low tempera-

tures. As temperature increases, phonon scattering destroys the net magnetic moment of free and bonded radicals.[28] It is difficult to achieve a long range coupling of localized spin (at higher temperature) due to delocalization of electrons. The room temperature ferromagnetism in GO for functional applications can be achieved by the introduction of impurities of high spin state transition metals.[31]

Herein, we demonstrate single-step facile routes for the rapid synthesis of bifunctional Mn^{2+} bonded GO and RGO hybrid materials with a pronounced and tunable PL phenomenon in a wider wavelength range. The synthesis was carried out using the modified Hummer's method combined with a solvothermal reduction method. Mn^{2+} bonded GO and RGO afforded intimate bonding and synergetic coupling effects, leading to significantly higher PL in GO as compared to RGO. The enhancement of PL is induced by an Mn^{2+} mediated energy transfer process which is identified by the long decay lifetime. The X-ray photo spectroscopy revealed the covalent coupling of Mn^{2+} with GO/RGO, suggesting that these hybrid materials offer a promising strategy for advanced optoelectronics and bio-medical devices. To the best of our knowledge, this is the first report describing the bifunctional Mn^{2+} bonded GO and RGO hybrid materials for PL and magnetic properties. A detailed explanation of the origin of variable energy PL in Mn^{2+} bonded GO and RGO hybrid composites and the effect of pH on the optical properties have been presented in detail and we also reported the room-temperature ferromagnetism in GO which provides guidelines for the design of more subtle magnetic carbon devices.

2. Experimental

2.1 Synthesis of Mn^{2+} bonded graphene oxide and Mn^{2+} bonded reduced graphene oxide 2D nanosheet composites

The Mn^{2+} bonded graphene oxide and Mn^{2+} bonded reduced graphene oxide 2D nanosheet composites were synthesized using a facile and inexpensive technique. Initially, GO was prepared using natural graphite powders by the modified Hummer's method.[32] The GO water suspension (100 mL, 0.5 mg mL^{-1}) with 0.0079 g of $KMnO_4$ powders was first ultrasonicated for 1 h and then stirred for 15 min. The obtained solution was kept in an oven at 60 °C for 3 h and cooled to room temperature. After carefully filtering and washing with de-ionized water and alcohol, the intermediate product was then dispersed in de-ionized water. 30 mL of the supernatant was poured into a round bottom flask and heated at 200 °C for 12 h. The black precipitate was dispersed ultrasonically in de-ionized water and the suspension was further dialyzed in a dialysis bag overnight at a temperature of ~4 °C. The as-synthesized MnO_2 decorated GO product is obtained as an intermediate product in which MnO_4 is converted into MnO_2. Further, for Mn^{2+} complexation with the GO and RGO lattice, we added COOH (10 mL) in the intermediate product. This carboxyl group is reacted with MnO_2 nanoparticles in the presence of heated H_2O. Then, this functional group is removed

after reaction and meanwhile, Mn^{2+} ions are bonded/complexed with the available oxygen functionality in the GO and RGO lattice. It is also confirmed by the spectroscopy technique as well as high resolution microscopy as a metal contrast image of Mn clusters in the graphene lattice. Similar observations have been previously reported for Eu, Pt or Au atoms on the graphene lattice or carbon nanotubes.[33,34] The pH was controlled by adding an aqueous solution of NaOH dropwise into the solution and simultaneously measuring the pH using a pH meter. The effect of pH on the optical properties has been studied in detail. Henceforth, the Mn^{2+} bonded GO (MnGO) and Mn^{2+} bonded RGO (MnRGO) two dimensional (2D) nanosheet composite samples prepared at different pH values (4, 7 and 10) will be designated for Mn^{2+} bonded GO nanosheet composites as (MnGO4, MnGO7, and MnGO10) and for Mn^{2+} bonded RGO nanosheet composites as (MnRGO4, MnRGO7, and MnRGO10), respectively.

2.2 Characterization

X-ray diffraction studies of the powder samples have been carried out using Rigaku, Miniflex, CuKα; λ = 1.5405 Å. Prior to the XRD measurement, the diffractometer was calibrated using silicon powder as the reference material (d_{111} = 3.1353 Å).[35] The accurate lattice parameters were also obtained through the least squares fitting method using computer-based unit cell refinement software.[36] Raman studies were carried out using an argon ion laser with a wavelength of 514.5 nm as the excitation source (Model Innova 70, Coherent). FTIR spectroscopic measurements were performed on a Thermo Scientific FTIR spectrometer (model: NICOLET 6700). The spectra were recorded at a resolution of 2 cm^{-1} and each spectrum was an average of 32 scans. The XPS analysis was performed in an ultra-high vacuum (UHV) chamber equipped with a hemispherical electron energy analyzer (Perkin Elmer, PHI1257) using a non-monochromatized Al Kα source (excitation energy of 1486.7 eV) with a base pressure of 4×10^{-10} torr at room temperature. The surface morphology and microstructural characterization were carried out by using a scanning electron microscope (SEM, model no. EVO MA 10 VPSEM) and a high resolution transmission electron microscope (HRTEM, model no. Technai G20-twin, 200kv with super twin lenses having point and line resolution of 0.144 nm and 0.232 nm, respectively) equipped with energy-dispersive X-ray spectroscopy (EDX) facilities for elemental studies. The chemical composition of MnGO10 nanosheet composites was analyzed by using an electron energy-loss spectrometer (EELS) using a spectrometer attached to the transmission electron microscope. UV-visible spectra were recorded using a high resolution UV-Vis spectrophotometer (model no. LS 55). The photoluminescence (PL) characterization was performed using a photoluminescence spectrometer (Edinburgh FLSP-920) equipped with a xenon lamp as an excitation source. The time resolved PL (TRPL) spectroscopy measurements were carried out using an Edinburgh luminescence spectrometer (F900) equipped with a microsecond xenon flash lamp as the source of excitation. Magnetic measurement has been performed to investigate the magnetic properties of Mn^{2+} bonded GO nanosheets using a SQUID-VSM (SVSM, Quantum Design Inc., USA) instrument.

3. Results and discussion

To analyse the crystalline structure of as-synthesized samples, XRD studies were carried out. The XRD patterns of MnGO10 and MnRGO10 composites are shown in Fig. 1a. The most intense diffraction peak of GO (black curve) at ~10.4° with a larger d-spacing (d = 0.865 nm) corresponds to the (001) reflection, which is characteristic of stacked GO sheets. The interlayer d-spacing of GO is significantly larger compared to that of 0.34 nm for pristine graphite due to the attachment of oxygen-containing functional groups on both sides of graphene sheets.[37] Thus, from the XRD pattern of MnGO10, it could be revealed that the original graphite powder has been almost completely oxidized. The XRD pattern of MnRGO10 composites (RGO is exfoliated into individual platelets by the chemical reduction of GO) shows a very broad reflection at ~23.1° as shown in Fig. 1a (red curve). The shift of the characteristic diffraction peak of graphite from 26.58° to 23.1° is due to the presence of short-range order in the stacked stacks. The interlayer spacing of RGO was 0.345 nm, which is slightly larger than that of graphite, due to the presence of a small amount of residual oxygen-containing functional groups or other structural defects.[38] The particle size of MnGO10 and MnRGO10 composites is estimated by Schemer's formula. The average sheet size of MnGO10 and MnRGO10 composites is found to be 150 and 300 nm, respectively. Besides these representative diffraction peaks of GO and RGO, no other peaks belonging to Mn is detected in the XRD patterns. This is ascribed to the low amount of Mn in the composite samples uniformly dispersed and encapsulated in GO and RGO nanosheets (instead of being agglomerated) as revealed by microscopic observations.

Raman spectroscopy is considered to be a very convenient and nonvolatile technique for information about the structure of the graphene sheets and their composites. The structural changes occurring during the chemical processing (from GO to RGO nanosheets) have been characterized using Raman spectroscopy. The Raman spectral profile for MnGO10 (black curve) and MnRGO10 (red curve) composites is shown in Fig. 1b. The Raman spectra displayed two remarkable peaks at 1350 and 1580 cm^{-1}, corresponding to the well documented D and G bands, respectively. Here, the D band is associated with the structural defects and disorder carbon in the graphitic layers, whereas the G band corresponds to the E_{2g} mode of sp^2-hybridized C–C bonds in a two-dimensional hexagonal lattice.[39] The intensity of the two peaks depends on the sp^2/sp^3 ratio.[40] Moreover, the relative strength of the D band compared to the G band usually signifies a higher degree of disorder related to exfoliation and the extent of defects in the graphitic materials.[41] The size of the sp^2 domains increases during the reduction of GO.[42] As shown in Fig. 1b, the I_D/I_G ratio gets reduced slightly from ~1.01 for MnRGO10 composites to
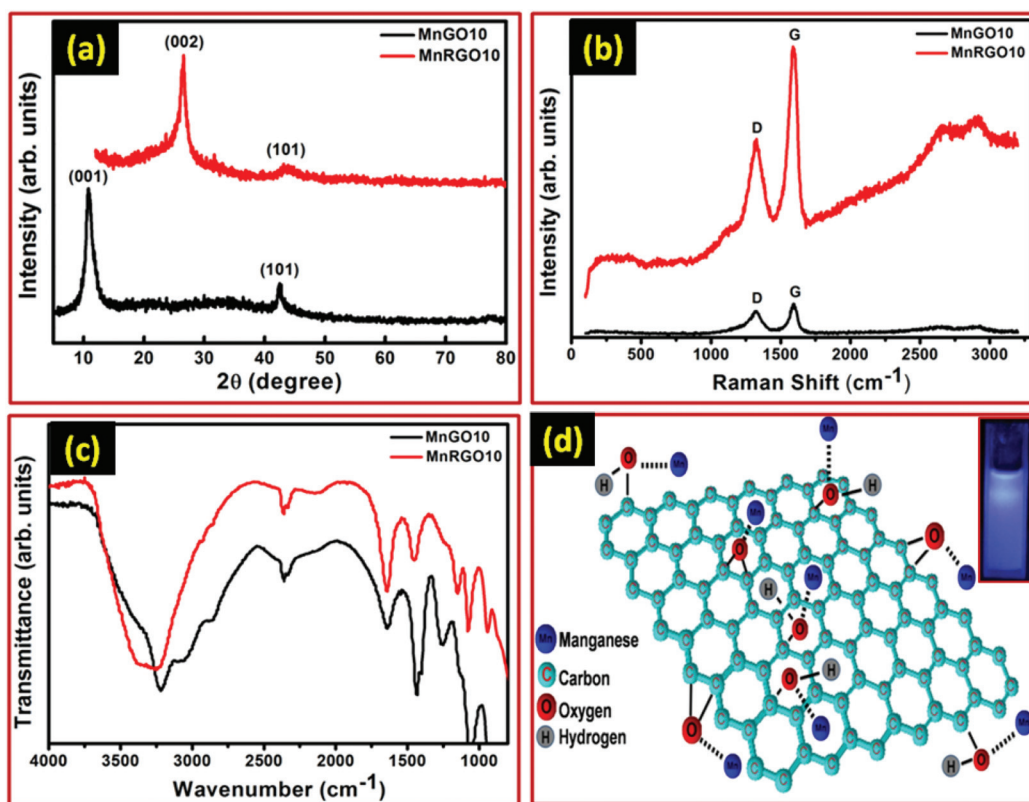
Fig. 1 (a) XRD spectra of MnGO10 and MnRGO10 composites, (b) Raman spectra of MnGO10 and MnRGO10 composites, (c) FTIR spectra of MnGO10 and MnRGO10 composites and (d) the plausible schematic model for MnGO10 composites, represents the bonding of the Mn^{2+} to the GO nanosheet lattices, inset shows the optical photograph of the MnGO10 composite suspension in a cuvette excited by wavelengths of a 310 nm portable UV lamp, showing that the blue emission is largely enhanced.

~0.92 for MnGO10 composites, due to the decrease in the average size of in-plane sp^2 domains, an increase of the edge planes, as well as the expansion of the disorder during the reduction of exfoliated GO, indicating the conversion of GO into RGO nanosheets.[43] There are no peaks corresponding to Mn or its compounds in the Raman spectra of MnGO10 and MnRGO10 composites, which is consistent with the XRD data. The FTIR spectral measurements have been used for further confirmation of the reduction of oxygen containing functional groups of GO and to investigate the bonding composition of the as-synthesized samples. Fig. 1c shows the FTIR spectra of MnGO10 (black curve) and MnRGO10 (red curve) composite samples. The FTIR spectrum of MnGO10 shows the presence of different types of oxygen functionalities in GO; such as, oxygen stretching vibration (3370 cm^{-1}, –OH vibration), C=O stretching vibration (1720 cm^{-1}), C–OH stretching vibration (1500 cm^{-1}), and C–O stretching vibration (1460 cm^{-1}). Importantly, the recorded FTIR spectrum clearly shows the presence of oxygen containing functional groups and also confirms that the oxygen groups have not been removed from the graphene basal plane. Moreover, the signature of the aromatic C=C stretching vibration of graphitic domains at ~1600 cm^{-1} indicates the presence of a sp^2 hybridized honeycomb lattice. In the case of the MnRGO10 composite spectrum, few modes are suppressed because of the reduction of GO into RGO. This implies that most of the carboxyl groups have been removed by the solvothermal treatment. Based on the above results, a schematic model of proposed bonding of the Mn^{2+} to the GO nanosheet lattices is shown in Fig. 1d. The inset of Fig. 1d displays the optical photograph image of an MnGO10 suspension kept in a cuvette and excited by a 310 nm portable UV lamp. The optical photo was taken by using a Nikon high-resolution digital camera and it reveals that the blue emission is largely enhanced.

The morphologies of Mn^{2+} bonded GO/RGO composite samples were investigated using SEM and TEM. Fig. 2a shows the SEM image of free-standing MnGO10 nanosheet composites consisting of crumpled and rippled structures closely associated with each other, which might be attributed to the defective structure formed due to the exfoliation and restacking processes. The MnRGO10 nanosheet composites, however, are layer structured, irregular and folded, as shown in the SEM image of Fig. 2b and c. Fig. 2c is a high-magnification view of Fig. 2b. These nanosheets are entangled with each other. The SEM images revealed that the dimension of MnGO10 and MnRGO10 nanosheets are about 150 and 300 nm, respectively. The dark contrast embedded on layers shows the presence of MnO_2 particles on the graphene sheets (Fig. 2a and c), which
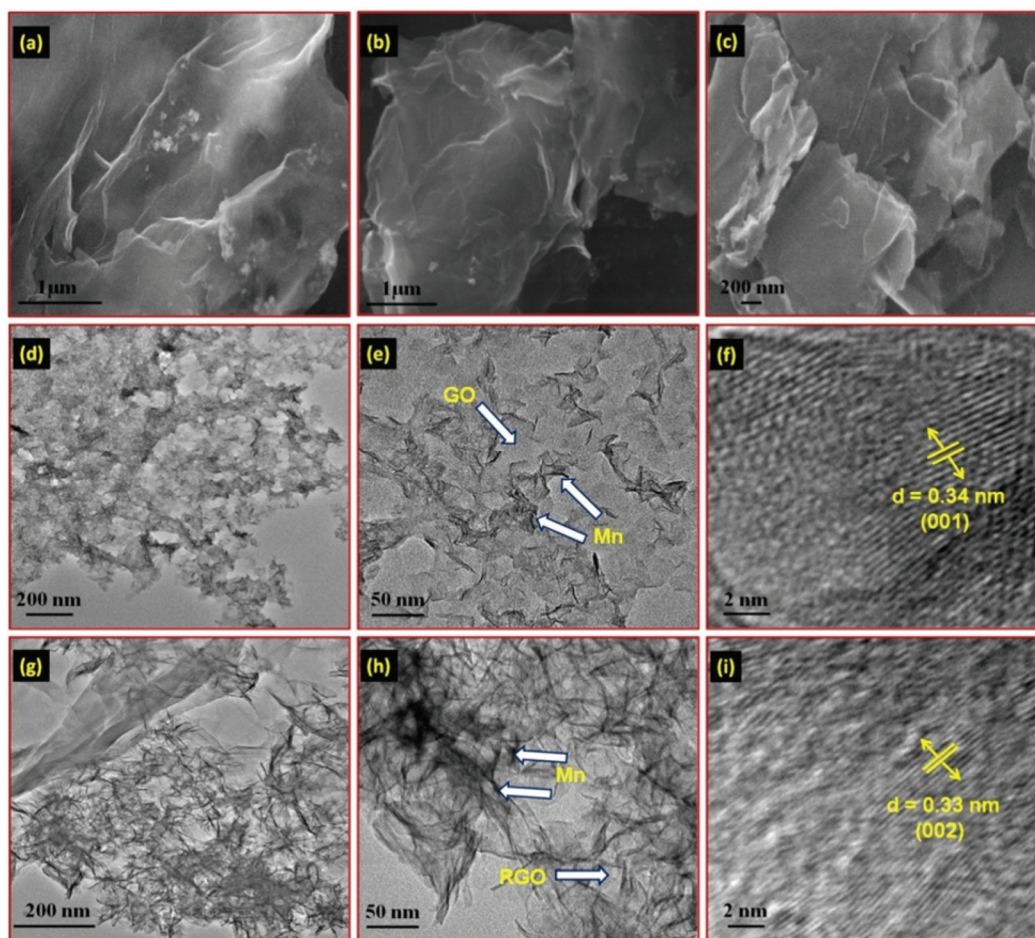
Fig. 2 (a) SEM image of MnGO10 nanosheet composites, (b) SEM image of MnRGO10 nanosheet composites, (c) magnified view of (b), (d) TEM image of MnGO10 nanosheet composites, (e) magnified view of (d); arrows represent the presence of MnO_2 particles on 2D graphene oxide nanosheets with black dotted structure and graphene oxide nanosheets, (f) HRTEM image of MnGO10 nanosheet composites, (g) TEM image of MnRGO10 nanosheet composites, (h) magnified view of (g); arrows represent the presence of MnO_2 particles on 2D reduced graphene oxide nanosheets with black dotted structure and reduced graphene oxide nanosheets and (i) HRTEM image of MnRGO10 nanosheet composites.

is further confirmed by TEM/HRTEM studies. It can be seen that MnO_2 decorates the surface of GO/RGO nanosheets and the folding and wrinkling characters of graphene sheets are well preserved. As shown in Fig. 2d and e (TEM observation of MnGO10 nanosheets) MnO_2 is well bonded to the GO nanosheets. Fig. 2g and h show the TEM images of single- or few-layered MnRGO10 nanosheets, which are transparent and have lots of wrinkles. Corrugation and scrolling suggest the intrinsic nature of graphene. The existence of 2D graphene sheets is shown with arrows in Fig. 2e and h. The Mn^{2+} ions bonded over the few layers of graphene sheet is clearly seen as black dots in the image (Fig. 2e and h). Through first-principles calculations, it has been shown that 3d-transition metal atoms have a covalent bonding with graphene due to the hybridization between the $d_{x^2-y^2}$ and d_{yz} orbitals of the metal atoms and p_z orbitals of the carbon atoms. The high affinity of these metal atoms to the non-perfect and strained regions of graphene sheets allows one to bind the metal atoms to the graphene, and these in effect tailor the properties of graphene or

carbon based materials. Thus, the bonding of MnO_2 particles to the GO/RGO nanosheets significantly transfers the efficient energy. The high-resolution TEM images of MnGO10 and MnRGO10 composites (Fig. 2f and i) show the lattice fringes with the d spacing of ∼0.34 nm and ∼0.33 nm, corresponding to the (001) and (002) planes of GO and RGO, respectively, which are consistent with the XRD pattern. This is further confirmed by the presence of Mn^{2+} ions bonded to the GO and RGO nanosheets as shown through the XPS studies. The cluster size of Mn (>1 nm) in Mn^{2+}-bonded in the graphene lattice can be realized from metal cluster contrast images from Fig. 2f and i.

To understand the composition and chemical nature of MnGO10 and MnRGO10 composite samples, XPS measurements have been performed (Fig. S1; see ESI†). The XPS survey spectra of MnGO10 and MnRGO10 composites are shown in Fig. S1a and S1c,† respectively, indicating the presence of carbon, oxygen and Mn elements. No other element was detected. These results further confirmed the insufficient
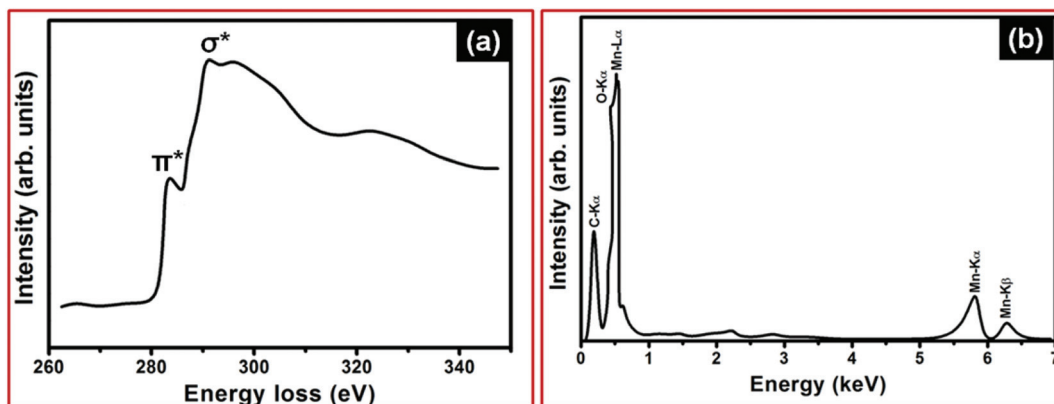
Fig. 3 (a) EELS and (b) EDX spectra of MnGO10 nanosheet composites.

reduction of GO by the chemical reduction method, which is consistent with the results of XRD. The high resolution spectra of the C 1s region for MnGO10 and MnRGO10 composites are shown in Fig. S1b and S1d,† respectively. The differences between the C 1s spectra of MnGO10 and MnRGO10 are evident from the shape and peak identity. XPS analysis demonstrated that the main peak positioned at about 284.6 eV is due to the non-oxygenated carbon atom ring (sp^2 C–C bond), while the other peaks at 286.7, 287.8 and 289.1 eV correspond to the oxygen containing groups (C–OH), (C=O) and (O=C–OH), respectively (Fig. S1b†). However, according to C 1s spectra analysis of MnRGO10 in Fig. S1d,† after the chemical reduction of GO, the intensity of the characteristic peaks for the oxygen containing functional groups significantly decreased, though they did not completely vanish, which is in good agreement with FTIR results. A significantly larger proportion of oxygen in GO existed in the form of C–O functionalities and a smaller proportion of oxygen is associated with the hydroxyl and O–C=O groups. The peaks of oxygen-containing groups at 284.5 eV (C–O), 286.8 eV (C=O), and 289 eV (O–C=O) decreased to different degrees. The proportion of the C=O group decreased greatly and the O–C=O group vanished, while the proportions of hydroxyl groups changed slightly, demonstrating that the chemical reduction method has little effect on the deoxygenation of hydroxyl groups. The core level peak of O 1s for MnGO10 composites is shown in Fig. S1e,† peaking at 532.1 eV binding energy. The Mn 2p XPS spectra acquired from the synthesized composite product confirmed the existence of MnO$_2$. The high resolution core level peaks of Mn 2p for MnGO10 and MnRGO10 composites are shown in Fig. S1f and S1g,† respectively. Only a single peak appeared at ~641.3 eV corresponding to Mn 2p$_{3/2}$ and two symmetrical peaks at ~641.6 eV and ~656 eV corresponding to Mn 2p$_{3/2}$ and Mn 2p$_{1/2}$ for MnGO10 and MnRGO10 composites, respectively are presented. The spin orbit splitting between Mn 2p$_{3/2}$ and Mn 2p$_{1/2}$ is ~14.4 eV, suggesting the formation of MnO$_2$ and corresponds to the 2p binding energy of Mn^{2+} ions. The oxidation properties of manganese, Mn 2p peak positions and solubility of Mn^{2+} ions in acid alkali solutions indicate that at all mentioned pH values, Mn^{2+} ions remain bonded to the surface of all as-synthesized composites related to GO and RGO nanosheets. Furthermore, electron energy loss spectroscopy (EELS), and energy dispersive X-ray spectroscopy (EDX) were used to study the elemental analysis, structure and chemistry of the as-prepared composite samples. The EELS and EDX spectra of MnGO10 nanosheet composites are shown in Fig. 3a and b. It indicates the presence of C, O and Mn elements in the as-synthesized composites as well as the formation of an Mn^{2+} ions complex in the honeycomb carbon lattice.

The UV–vis absorption spectra of MnGO10 and MnRGO10 composites dispersed in water are shown in Fig. 4a. As can be seen from Fig. 4a, the absorption peak of MnGO10 is in the range of 231 to 270 nm. A typical absorption peak at approximately 250 nm arises due to the π–π* transition of C–C and C=C bonds in sp^2 hybrid domain regions, and a shoulder peak observed at approximately 300 nm is due to the π–π* transition of the C=O bond in sp^3 hybrid regions. Whereas, the absorption peak of RGO is shifted towards the blue wavelength region, which may be attributed to the exfoliation of layered GO sheets during the synthesis process.[12,44]

To explore the optical properties of MnGO10 and MnRGO10 composite samples, a detailed PL study was carried out at room temperature. The new interesting enhanced PL behavior is observed in as-synthesized MnGO10 and MnRGO10 composites.

It is well known that the intrinsic and tunable fluorescence from GO or RGO could offer exciting and previously unforeseen optical applications for graphene-based materials. The strongly heterogeneous atomic and electronic structures of GO indicate that the fluorescence in GO arises from the recombination of electron–hole pairs in localized electronic states originating from various possible configurations, rather than from band-edge transitions similar to the case of typical semiconductors. In order to understand the wavelength dependence and the excitation wavelength at which the PL intensity is maximum, the PL emission and excitation spectra for MnGO10 and MnRGO10 composites are carried out and the results are shown in Fig. S2 (see ESI†). An enhanced and
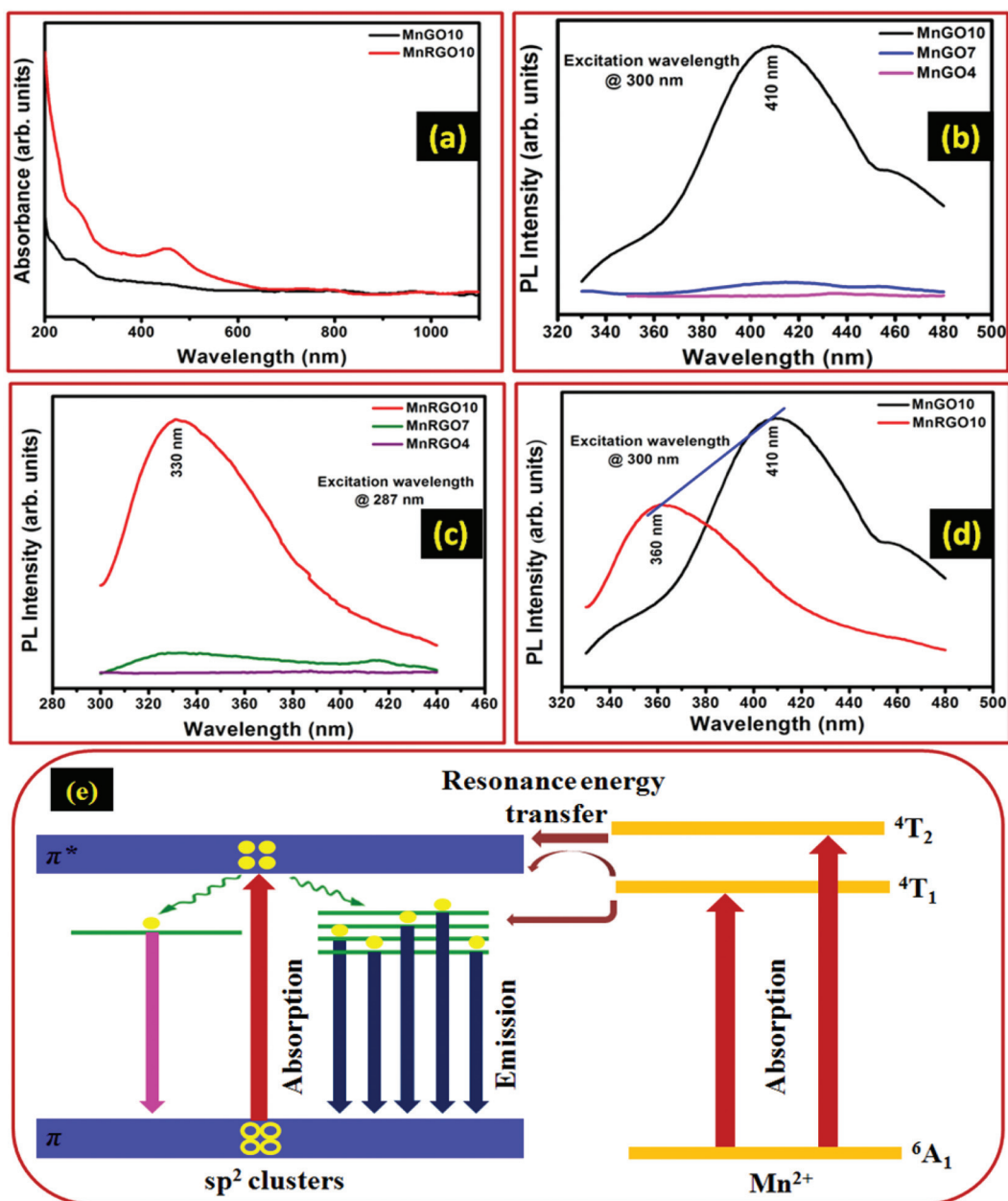
Fig. 4 (a) UV−vis absorption spectra of MnGO10 and MnRGO10 composites, pH dependence PL spectra for (b) MnGO, (c) MnRGO composites having different pH values (4, 7 and 10), (d) dependence of PL blue-shift of the MnRGO10 composite samples compared to MnGO10 composites (represented by a solid blue line) on the value of sp^2 fractions and (e) plausible schematic mechanism energy-level diagram of MnGO10 composites explaining the PL emission in GO associated with the Mn^{2+} mediated energy transfer process; the blue emission is attributed to the 410 nm wavelength due to the $^4T_2$ to $^6A_1$ transition of Mn^{2+}. The energy transfer from Mn^{2+} to sp^2 clusters corresponds to variable and broad PL emissions.

tunable PL in the visible range is observed. The various PL emission spectra for MnGO10 composites were recorded at different excitation wavelengths ranging from 250 to 500 nm (Fig. S2a†). The PL peak position shifts towards the longer wavelength side by varying the excitation wavelength. A strong blue emission is obtained at 410 nm, when the sample is excited with 300 nm wavelength. It has been reported that isolated sp^2 clusters within the carbon–oxygen sp^3 matrix could yield band gaps consistent with blue emission due to the localization of electron–hole pairs.[17] The PLE spectra for MnGO10

composites at different emission wavelengths from 357 to 488 nm are shown in Fig. S2b.† It is observed that the excitation intensity is maximum at 315 nm wavelength under 418 nm emission wavelength.

Similarly, the corresponding PL and PLE spectra for MnRGO10 composites are displayed in Fig. S2c and S2d,† respectively. The emission wavelength remains centered at about 330 nm when the excitation wavelength is varied from 250 to 290 nm and the PL intensity also varies depending on the excitation wavelength (Fig. S2c†). When the excitation

wavelength was increased from 310 nm to higher values, the emission spectra shifted towards the longer wavelength region. The red shift observed in the PL spectra (with increasing excitation wavelengths) is essentially a quantum confinement effect related to the size of the sp^2 clusters. When the sample is excited by 287 nm, a broad emission with a maximum intense peak at 330 nm is observed. In addition, the PLE spectra of MnRGO10 composites at different emission wavelengths from 300 to 620 nm are also shown in Fig. S2d.† It is observed that at a 332 nm emission wavelength, a broad peak is obtained at 287 nm. At higher emission wavelengths from 395 to 620 nm, the PL intensity gets suppressed to a greater extent. The excitation wavelength dependence of the emission wavelength and intensity is a common phenomenon observed in carbon-based materials. The predominant broad emission band in the as-synthesized MnGO and MnRGO composite samples for a wide-range of excitation energies may be attributed to optical transitions from these disorder-induced localized states, emissive traps, electronic conjugate structures, and free zigzag sites.

The proposed PL mechanism based on the emissive free zigzag sites is further supported by the observed pH-dependent PL. The PL emission spectra of the MnGO composites with different pH values 4, 7 and 10 are shown in Fig. 4b. The PL emission of MnGO composites is very sensitive to pH values, having better fluorescence at higher pH values, and the emission wavelength does not shift with increase of pH value. For MnGO10, under an excitation wavelength of 300 nm, a high peak intensity is observed at a near-UV wavelength of 410 nm. It is well known that the blue PL originates from localized sp^2 domains within the sp^3 matrix.[17] The PL emission spectra for MnRGO composites at different pH values (4, 7 and 10) are shown in Fig. 4c. As can be seen in the figure, under an excitation wavelength of 287 nm, a broad band emission is observed at 330 nm. The fluorescence of carbon based materials is pH dependent. At higher pH values, the fluorescence is strong enough that it can be observed even by the naked eye, whereas it is nearly quenched at lower pH conditions. MnGO and MnRGO composites at different low pH values showed drastic suppression of the PL signal, which may be ascribed to the protonation of the emissive zigzag sites with the $\sigma^1\pi^1$ ground state under acidic conditions which quenches the fluorescence, whereas de-protonation under alkaline conditions recovers it. Thus, under alkaline conditions, the MnGO and MnRGO composites emit strong PL, whereas, under acidic conditions, the PL is nearly quenched. When pH is varied between 4 and 10, the PL intensity increases rapidly. The PLE spectra for MnGO and MnRGO composites at different pH values (4, 7 and 10) are also shown in Fig. S3a and S3b (see ESI†), respectively. Fig. 4d displays the PL emission spectra of MnGO10 and MnRGO10 composites. A strong PL emission from MnGO10 and a weak PL emission from MnRGO10 have been observed under the excitation by 300 nm laser light. For the MnGO10, the broad band emission in the 330–480 nm (short wavelength range) is observed and the main feature shifts toward shorter wavelengths (from 410 nm for MnGO10

to 360 nm for MnRGO10 composites). The emission peak position and width depend on the sp^2 fraction. Interestingly, the PL blue-shift is due to reduction of functional groups in MnRGO10 composites, as indicated by the solid blue line in Fig. 4d. It suggests that the increase in the sp^2 fraction may be responsible for the PL blue-shift of MnRGO10 composites and one can tailor the PL blue-shift by tuning the sp^2 fraction of the MnRGO10 composite samples. The PL of MnRGO10 composites shows the maximum blue-shift of approximately 50 nm. It can be noticed that in the case of graphene oxide having pH 10 (MnGO10), the intensity of emission and excitation spectra get enhanced compared to other samples. This may be due to efficient energy conversion from oxygen functionality to Mn^{2+} compared to the RGO lattice.

The plausible schematic mechanism explaining the PL from MnGO10 composites is illustrated in Fig. 4e. It is well known that (i) the optoelectronic properties of carbon based materials are mainly determined by the π and π^* states of the sp^2 sites which lie within the σ–σ^* gap and (ii) the PL emission of GO mainly originates from sp^2 clusters that are isolated within the sp^3 carbon–oxygen or defects. The RGO has a higher content of oxygen functional groups, suggesting that it consists of numerous disorder-induced defect states within the π–π^* gap.[23] It was proposed that (i) π bonding is weaker and has a lower formation energy than σ bonding; and (ii) a large number of disorder-induced localized states are in the two-dimensional networks of the RGO composite, which consists of a large fraction of distorted carbon atoms attached to oxygen-containing functional groups. After the reduction of GO into RGO, the number of disorder-induced states within the π–π^* gap decreases, and an increased number of cluster-like states from the newly formed isolated sp^2 domains are formed. Therefore, the electron–hole recombination among these sp^2 cluster-like states with variable bandgaps corresponds to the excitation-dependent emission by GO and RGO composites.

The variable PL emission for different excitation wavelengths for MnGO and MnRGO composites is due to the disorder-induced localized defect states at carbene-like zigzag sites. The introduction of Mn^{2+} ions is also associated with the mediated emission in GO and RGO composites, which corresponds to the $^4T_2$ to $^6A_1$ transition of Mn^{2+}. Since Mn^{2+} is bonded to the sp^2 clusters, the short distance and the energy level overlap lead to effective energy transfer from Mn^{2+} to the sp^2 clusters. As a result, the radiative recombination rate increased significantly and the PL spectra were consequently enhanced. When the excitation wavelength was shorter than 400 nm, the $^6A_1$ to $^4T_2$ mediated transition state of Mn^{2+} was gradually dominantly excited and the energy was transferred quickly to the sp^2 clusters in GO, resulting in the blue PL emission at 410 nm for MnGO composites. The emission by the synthesized composites occurs due to the presence of a large scale of sp^2 clusters and resonant energy transfer between Mn^{2+} and sp^2 clusters due to pH-dependent reversible solubility of Mn^{2+}-related salts. In addition, the broad PL emission at ~410 nm for MnGO composites is attributed to the light absorption by the broad energy gap of the sp^2 clusters. Hence,

the presence of the $^4T_2$ level of Mn^{2+} also causes the excited electrons to occupy the energy level situation at the 300 nm energy level. These electrons relax non-radiatively to the next lower level centered at 410 nm and radiative recombination occurs. The enhanced and broad PL peak centered at 410 nm can thus be mainly attributed to the introduction of Mn^{2+}. When the excitation wavelength longer than 400 nm is used, lower energy photons cannot be absorbed by Mn^{2+}, therefore, the PL intensity diminishes. The presence of Mn^{2+} energy levels causes effective absorption by few sp^2 clusters with low energy levels. The radiative recombination to the ground state, together with the process of transfer between Mn^{2+} and sp^2 clusters, produces enhanced PL. Since the transition probability of $^4T_2$ to $^6A_1$ from Mn^{2+} is much higher than that of $^4T_1$ to $^6A_1$, the 410 nm emission is the most intense. Moreover, the MnRGO composites may exhibit purple PL at shorter wavelengths. In other words, the reduction may increase the number of small sp^2 domains, resulting in the PL spectra of MnRGO composites shifting from blue to shorter wavelengths.

The decay lifetime is an important parameter to investigate the emission mechanism as well as for deciding the performance of materials for their suitable use. The efficiency of radiative recombination is directly proportional to the decay time of the particular transition. The luminescence decay curve of MnGO10 and MnRGO10 composites is shown in Fig. 5. It was measured at room temperature by a time-correlated single photon counting spectrometer with a microsecond xenon flash lamp as the source of excitation. The lifetime data obtained for MnGO and MnRGO composites were fitted to a triple-exponential function as,[45–47]

$$I(t) = A_1 \exp(-t/\tau_1) + A_2 \exp(-t/\tau_2) + A_2 \exp(-t/\tau_3) \qquad (1)$$

where τ_1, τ_2 and τ_3 are the decay lifetimes of the luminescence, and A_1, A_2 and A_3 are the weighting parameters. The radiative transition is observed at 410 nm with 300 nm excitation for MnGO10 composites and the decay profile is shown in Fig. 5a. Fig. 5b demonstrates the exponential fitting of decay profiles, as described in eqn (1) and the corresponding parameters generated from fitting are listed in the inset of Fig. 5b. The observed lifetimes are $\tau_1 \sim 5.8$ μs, $\tau_2 \sim 86.24$ μs and $\tau_3 \sim 348.37$ μs. The average lifetime for MnGO10 composites is $\tau_{av} \sim 304$ μs. The radiative transition is observed at 330 nm with a 287 nm excitation for MnRGO10 composites and the decay profile is shown in Fig. 5c. Fig. 5d demonstrates the exponential fitting of decay profiles, as described in eqn (1) and the corresponding parameters generated from fitting are listed in the inset of Fig. 5d. The observed lifetimes are $\tau_1 \sim 6.5$ μs, $\tau_2 \sim 36.4$ μs and $\tau_3 \sim 174.2$ μs. The average lifetime for MnRGO10 composites is $\tau_{av} \sim 156$ μs. It should be noted that the PL decay lifetime in MnGO10 is rather larger compared to
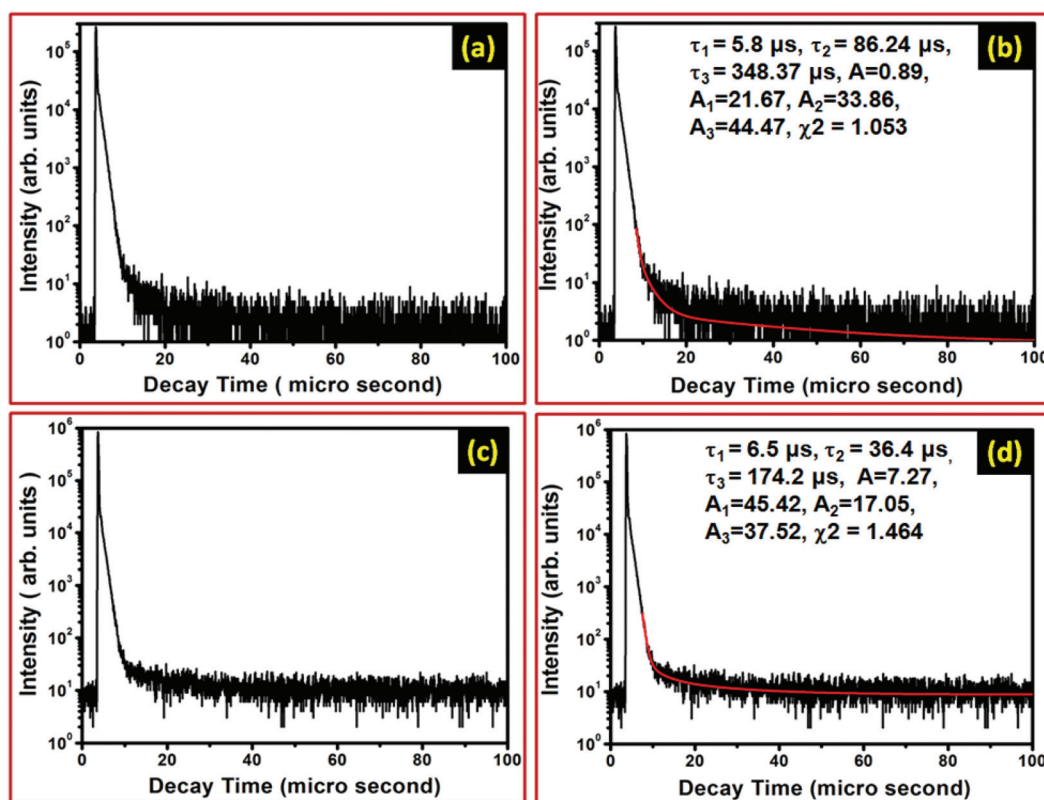

Fig. 5 (a) Time resolved PL decay profiles of MnGO10 composites recorded at room temperature, (b) the exponential fitting curves of MnGO10 composites with lifetime data parameters generated by exponential fitting, (c) time resolved PL decay profiles of MnRGO10 composites recorded at room temperature and (d) the exponential fitting curve of MnRGO10 composites with lifetime data parameters generated by exponential fitting.
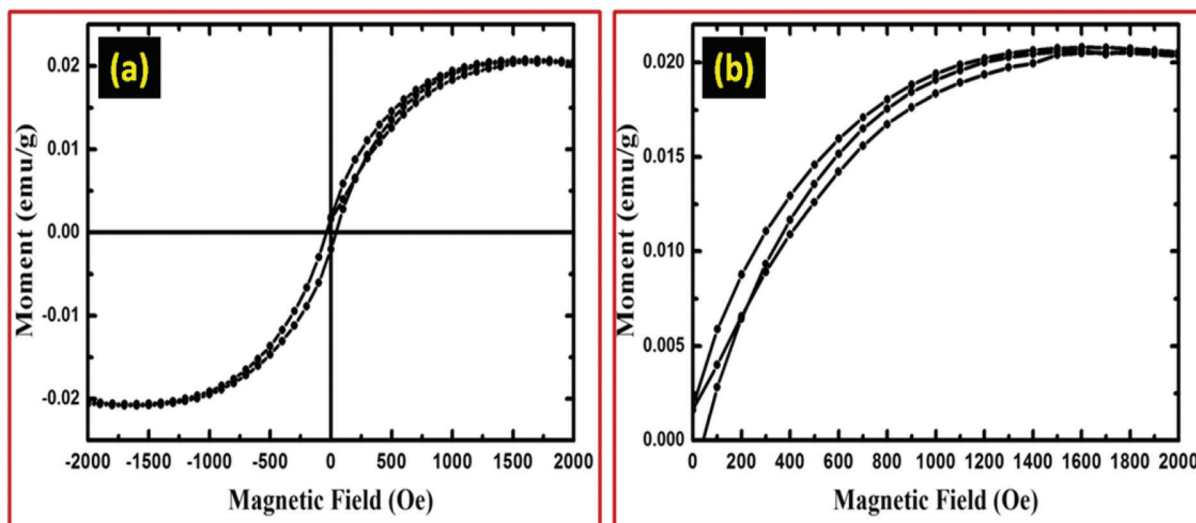
Fig. 6 (a) Magnetization of hysteresis loops at room temperature in the range of −2 kOe ≤ H ≤ +2 kOe for MnGO10 composites and (b) magnified view of (a) in the positive quadrant of magnetic field (from 0 kOe ≤ H ≤ +2 kOe).

MnRGO10 and the decay lifetime is of the order of micro-seconds. This long lifetime indicates the involvement of some extra charge carrier transport or recombination. Based on these observations, we proposed that Mn^{2+} acts as an intermediate state in the carrier decay process, which can well explain the observed long decay lifetime. The PL emission wavelength shifts towards shorter wavelengths (Fig. 4d). The intensity of the PL peak (MnGO) is higher than the peak of MnRGO composites. This longer emission wavelength exhibits a relatively long carrier lifetime.

The magnetization of hysteresis loops at room temperature in the range of −2 kOe ≤ H ≤ +2 kOe for MnGO10 composites is shown in Fig. 6a and its magnified view (the positive region of magnetic field from 0 kOe ≤ H ≤ +2 kOe) is depicted in Fig. 6b. The as-synthesized MnGO10 composite samples show weak ferromagnetism with saturation magnetization M_s = 0.020 emu g^{-1} at room temperature. The magnetization gets saturated at 1800 Oe for the sample. It is observed that the low spin state is more prominent in the flat geometry of graphene.[48] The doping concentration of Mn and the synthesis conditions (like oxygen environment) of the graphene oxide sample are optimized to stabilize the Mn^{2+} oxygen state. The covalently bonded oxygen atoms in one of the sub-lattice of GO and Mn ions generate the magnetic moment in GO clusters. The doping of Mn restores the damaged C conjugation and removes some OH and COOH groups through long range C–O–Mn bonding for long range magnetic ordering. The exchange interaction between the clusters have a notable impact on the magnetic moment of the doped GO system over a low energy difference and nano range.[49] Fig. 7 displays the isothermal magnetization data measured on MnGO10 composites at 77, 150, 300, 350 and 400 K with the magnetic field varying from −2 kOe to +2 kOe. Clear, s-shaped saturated open hysteresis loops (M(H)) curve) were observed at all the different

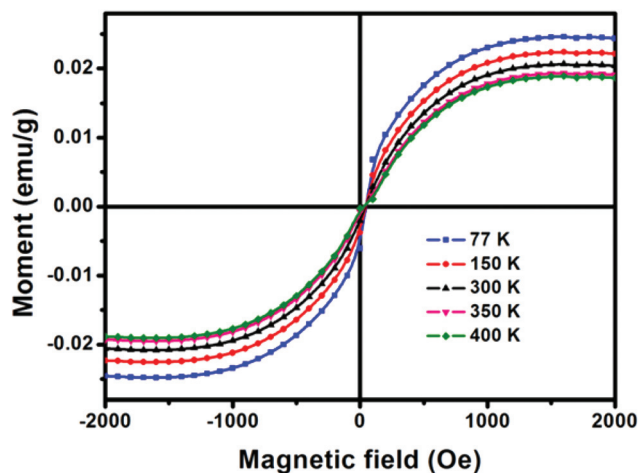**Fig. 7** Isothermal magnetization (M−H) observed on MnGO10 composites collected from H of −2 kOe to +2 kOe at various temperatures 77, 150, 300, 350 and 400 K.

temperatures measured including at 300 K, within the range of magnetization from ~0.024 to ~0.018 emu g^{-1}. It can be noticed that at lower temperatures, magnetic moments were enhanced as compared to room temperature as well as higher temperatures. Because, at higher temperatures, the phonon scattering destroys the net magnetic moment of the free and Mn^{2+}-bonded graphene lattice.

4. Conclusions

In summary, the luminomagnetic bifunctionality of Mn^{2+}-bonded graphene oxide/reduced graphene oxide two dimen-

sional nanosheets offers a new paradigm shift in the engineering of graphene analogs for tuning optical and magnetic properties. The manganese oxide nanoparticles are distributed over the wrinkled GO/RGO nanosheets. Ultraviolet-visible absorption spectroscopy results convincingly show the intercalation and adsorption of Mn^{2+} ions onto the GO/RGO sheets. The photoluminescence (PL) spectra excited by different wavelengths revealed that the resonant energy transfer between Mn^{2+} and sp^3/sp^2 clusters of GO/RGO is responsible for the enhancement of a broad range of wavelength emissions. This enhanced tunable PL is strongly related to the induced changes of their heterogeneous electronic structures and bonding properties. The weak longer wavelength emission is observed in Mn^{2+} bonded RGO as compared to Mn^{2+} bonded GO composites due to the hopping and tunneling effects which facilitated the migration of excitons to nonradiative recombination sites. Moreover, the complex pH-sensitive PL behaviors have also been examined. The ferromagnetic behavior occurs from the defects on Mn^{2+} bonded GO composites. We visualize that such accomplishments will be key to developing the much-awaited high performance applications of graphene and its analogs in the fields of various technological applications.

Acknowledgements

References

1 P. V. Kamat, *J. Phys. Chem. Lett.*, 2011, **2**, 242–251.

2 C. H. Chuang, Y. F. Wang, Y. C. Shao, Y. C. Yeh, D. Y. Wang, C. W. Chen, J. W. Chiou, S. C. Ray, W. F. Pong, L. Zhang, J. F. Zhu and J. H. Guo, *Sci. Rep.*, 2014, **4**, 4525.

3 H. Yamaguchi, G. Eda, C. Mattevi, H. Kim and M. Chhowalla, *ACS Nano*, 2010, **4**, 524–528.

4 C. T. Chien, S. S. Li, W. J. Lai, Y. C. Yeh, H. A. Chen, I. S. Chen, L. C. Chen, K. H. Chen, T. Nemoto, S. Isoda, M. Chen, T. Fujita, G. Eda, H. Yamaguchi, M. Chhowalla and C. W. Chen, *Angew. Chem., Int. Ed.*, 2012, **51**, 6662–6666.

5 S. Gilje, S. Han, M. Wang, K. L. Wang and R. B. Kaner, *Nano Lett.*, 2007, **7**, 3394–3398.

6 J. L. Li, H. C. Bao, X. L. Hou, L. Sun, X. G. Wang and M. Gu, *Angew. Chem., Int. Ed.*, 2012, **51**, 1830–1834.

7 R. J. W. E. Lahaye, H. K. Jeong, C. Y. Park and Y. H. Lee, *Phys. Rev. B: Condens. Matter*, 2009, **79**, 125435.

8 S. Saxena, T. A. Tyson and E. Negusset, *J. Phys. Chem. Lett.*, 2010, **1**, 3433–3437.

9 Z. Luo, P. M. Vora, E. J. Mele, A. T. C. Johnson and J. M. Kikkawa, *Appl. Phys. Lett.*, 2009, **94**, 111909.

10 C. Galande, A. D. Mohite, A. V. Naumov, W. Gao, L. Ci, A. Ajayan, H. Guo, A. Srivastava, R. B. Weisman and P. M. Ajayan, *Sci. Rep.*, 2011, **1**, 85.

11 J. L. Chen and X. P. Yan, *Chem. Commun.*, 2011, **47**, 3135–3137.

12 J. I. Paredes, S. Villar-Rodil, A. Martínez-Alonso and J. M. D. Tasćon, *Langmuir*, 2008, **24**, 10560–10564.

13 Z. Gan, S. Xiong, X. Wu, T. Xu, X. Zhu, X. Gan, J. Guo, J. Shen, L. Sun and P. K. Chu, *Adv. Opt. Mater.*, 2013, **1**, 926–932.

14 K. P. Loh, Q. Bao, G. Eda and M. Chhowalla, *Nat. Chem.*, 2010, **2**, 1015–1024.

15 T. Gokus, R. R. Nair, A. Bonetti, M. Bohmler, A. Lombardo, K. S. Novoselov, A. K. Geim, A. C. Ferrari and A. Hartschuh, *ACS Nano*, 2009, **3**, 3963–3968.

16 Z. Luo, P. M. Vora, E. J. Mele, A. T. C. Johnson and J. M. Kikkawa, *Appl. Phys. Lett.*, 2009, **94**, 111909.

17 G. Eda, Y. Y. Lin, C. Mattevi, H. Yamaguchi, H. A. Chen, I. S. Chen, C. W. Chen and M. Chhowalla, *Adv. Mater.*, 2010, **22**, 505–509.

18 D. Y. Pan, J. C. Zhang, Z. Li and M. H. Wu, *Adv. Mater.*, 2010, **22**, 734–738.

19 J. Du, X. Y. Lai, N. L. Yang, J. Zhai, D. Kisailus, F. B. Su, D. Wang and L. Jiang, *ACS Nano*, 2011, **5**, 590–596.

20 Y. Y. Liang, Y. G. Li, H. L. Wang, J. G. Zhou, J. Wang, T. Z. Regier and H. J. Regier, *Nat. Mater.*, 2011, **10**, 780–786.

21 Z. S. Wu, W. C. Ren, D. W. Wang, F. Li, B. L. Liu and H. M. Cheng, *ACS Nano*, 2010, **10**, 5835–5842.

22 Q. S. Mei, K. Zhang, G. J. Guan, B. H. Liu, S. H. Wang and Z. P. Zhang, *Chem. Commun.*, 2010, **46**, 7319–7321.

23 Z. X. Gan, S. J. Xiong, X. L. Wu, C. Y. He, J. C. Shen and P. K. Chu, *Nano Lett.*, 2011, **11**, 3951–3956.

24 H. Li, H. He, T. Zhang, L. Sun and Z. Ye, *RSC Adv.*, 2014, **4**, 54832–54836.

25 X. Yang, H. Xia, X. Qin, W. Li, Y. Dai, X. Liu, M. Zhao, Y. Xia, S. Wang and B. Yan, *Carbon*, 2009, **47**, 1399–1406.

26 K. S. Novoselov, A. K. Geim, S. V. Morozov, D. Jiang, Y. Zhang, S. V. Dubonos, I. V. Grigorieva and A. A. Firsov, *Science*, 2004, **306**, 666–669.

27 L. Li, R. Qin, H. Li, L. Yu, Q. Liu, G. Luo, Z. Gao and J. Gao, *ACS Nano*, 2011, **5**, 2601–2610.

28 R. McIntosh, M. A. Mamo, B. Jamieson, S. Roy and S. Bhattacharyya, *Europhys. Lett.*, 2012, **97**, 38001.

29 Y. Wang, Y. Huang, Y. Song, X. Zhang, Y. Ma, J. Liang and Y. Chen, *Nano Lett.*, 2009, **9**, 220–224.

30 H. S. S. Ramakrishna Matte, K. S. Subrahmanyam and C. N. R. Rao, *J. Phys. Chem. Lett.*, 2009, **113**, 9982–9985.

31 J. Barzola-Quiquia, R. Hohne, M. Rothermel, A. Setzer, P. Esquinazi and V. Heera, *Eur. Phys. J. B*, 2008, **61**, 127–130.

32 W. S. Hummers and R. E. Offeman, *J. Am. Chem. Soc.*, 1958, **80**, 1339–1339.

33 B. K. Gupta, P. Thanikaivelan, T. N. Narayanan, L. Song, W. Gao, T. Hayashi, A. L. M. Reddy, A. Saha, V. Shanker,

M. Endo, A. A. Marti and P. M. Ajayan, *Nano Lett.*, 2011, **11**, 5227–5233.

34 Y. Gan, L. Sun and F. Banhart, *Small*, 2008, **4**, 587–591.

35 G. Kedawat, S. Srivastava, V. K. Jain, P. Kumar, V. Kataria, Y. Agrawal, B. K. Gupta and Y. K. Vijay, *ACS Appl. Mater. Interfaces*, 2013, **5**, 4872–4877.

36 B. K. Gupta, D. Haranath, S. Saini, V. N. Singh and V. Shanker, *Nanotechnology*, 2010, **21**, 055607.

37 X. Tong, H. Wang, G. Wang, L. Wan, Z. Ren and J. J. Bai, *Solid State Chem.*, 2011, **184**, 982–989.

38 W. Gao, L. B. Alemany, L. Ci and P. M. Ajayan, *Nat. Chem.*, 2009, **1**, 403–408.

39 K. N. Kudin, B. Ozbas, H. C. Schniepp, R. K. Prud'homme, I. A. Aksay and R. Car, *Nano Lett.*, 2008, **8**, 36–41.

40 A. C. Ferrari, *Solid State Commun.*, 2007, **143**, 47–57.

41 Y. Y. Wang, Z. H. Ni, T. Yu, Z. X. Shen and H. M. Wang, *J. Phys. Chem. C*, 2008, **112**, 10637–10640.

42 J. Gao, F. Liu, Y. Liu, N. Ma, Z. Wang and X. Zhang, *Chem. Mater.*, 2010, **22**, 2213–2218.

43 A. C. Ferrari, J. C. Meyer, V. Scardaci and C. Casiraghi, *Phys. Rev. Lett.*, 2006, **97**, 187401.

44 Z. Ai, L. Zhang, F. Kong, H. Liu, W. Xing and J. Qiu, *Mater. Chem. Phys.*, 2008, **111**, 162–167.

45 J. Dwivedi, P. Kumar, A. Kumar, Sudama, V. N. Singh, B. P. Singh, S. K. Dhawan, V. Shanker and B. K. Gupta, *RSC Adv.*, 2014, **4**, 54936–54947.

46 B. K. Gupta, T. N. Narayanan, S. A. Vithayathil, Y. Lee, S. Koshy, A. L. M. Reddy, A. Saha, V. Shanker, V. N. Singh, B. A. Kaipparettu, A. A. Martí and P. M. Ajayan, *Small*, 2012, **8**, 3028–3034.

47 B. K. Gupta, V. Rathee, T. N. Narayanan, P. Thanikaivelan, A. Saha, Govind, S. P. Singh, V. Shanker, A. A. Marti and P. M. Ajayan, *Small*, 2011, **7**, 1767–1773.

48 M. Sepioni, S. Rablen, R. R. Nair, J. Narayanan, F. Tuna, R. Winpenny, A. K. Geim and I. V. Grigorieva, *Phys. Rev. Lett.*, 2010, **105**, 207205.

49 D. W. Boukhvalov and M. I. Katsnelson, *ACS Nano*, 2011, **5**, 2440–2446.